PHOTONICS Research

Ultrasensitive terahertz metamaterial sensor based on vertical split ring resonators

Wei Wang,[1] Fengping Yan,[1,*] Siyu Tan,[1] Hong Zhou,[2] and Yafei Hou[3]

[1]Key Laboratory of All Optical Network & Advanced Telecommunication of EMC, Institute of Lightwave Technology, Beijing Jiaotong University, Beijing 100044, China
[2]Department of Electronics, Information and Communication Engineering, Osaka Institute of Technology, 5-16-1 Omiya, Asahi-ku, Osaka 535-8585, Japan
[3]Graduate School of Natural Science and Technology, Okayama University, 1-1-1 Tsushimanaka, Kita Ward, Okayama Prefecture 700-8530, Japan
*Corresponding author: fpyan@bjtu.edu.cn

Received 7 July 2017; revised 13 September 2017; accepted 15 September 2017; posted 15 September 2017 (Doc. ID 301871); published 16 October 2017

An ultrasensitive metamaterial sensor based on double-slot vertical split ring resonators (DVSRRs) is designed and numerically calculated in the terahertz frequency. This DVSRR design produces a fundament *LC* resonance with a quality factor of about 20 when the incidence magnetic field component normal to the DVSRR array. The resonant characteristics and sensing performance of the DVSRR array design are systematically analyzed employing a contrast method among three similar vertical split ring resonator (SRRs) structures. The research results show that the elimination of bianisotropy, induced by the structural symmetry of the DVSRR design, helps to achieve *LC* resonance of a high quality factor. Lifting the SRRs up from the substrate sharply reduces the dielectric loss introduced by the substrate. All these factors jointly result in superior sensitivity of the DVSRR to the attributes of analytes. The maximum refractive index sensitivity is 788 GHz/RIU or 1.04×10^5 nm/RIU. Also, the DVSRR sensor maintains its superior sensing performance for fabrication tolerance ranging from −4% to 4% and wide range incidence angles up to 50° under both TE and TM illuminations.

OCIS codes: (160.3918) Metamaterials; (280.4788) Optical sensing and sensors.

https://doi.org/10.1364/PRJ.5.000571

1. INTRODUCTION

Metamaterials have been a hot topic among the scientific community for nearly two decades. In the first several years, a large number of theoretical and modeling achievements sprung up one after another, like methods for determination and characterization of the effective parameters for various metamaterial structures [1–6]. From then on, research interests gradually turned to applications, such as superlenses, high refractive index (RI) materials [7], perfect absorbers [8], and antireflection coating [9]. This is because metamaterials have extraordinary properties that are inaccessible in natural materials. This unique advantage offers metamaterials the capacity to independently manipulate their effective parameters, i.e., permittivity and permeability, through adjusting the shape and configuration of their metal or/and dielectric constituents [1,2]. In particular, the controllable permeability of metamaterials, namely, the magnetic activity, plays a vital role in the implementation of various devices in the higher parts of the electromagnetic (EM) spectrum [10–12], since the magnetism tends to vanish in the terahertz and higher frequencies.

Experimental realization of metamaterial devices starts from microwave frequencies [13]. In the lower frequency range, a strong magnetic response to impinging light can be obtained by the incidence magnetic field vertically crossing over split ring resonators (SRRs) [2]. However, this approach cannot work well in the terahertz and higher frequency bands, because SRR arrays at these frequencies, in general, can be processed only on the plane with the incidence light illuminating from the top of the plane due to fabrication technological limitations [10,11]. In such configurations, the direction of the magnetic moment, if it occurs, induced by the SRR array is not parallel or antiparallel to the driving magnetic field component, and, therefore, the magnetic response is weak or even nonexistent. Fortunately, in recent years, the vertical SRR (VSRR) had been analyzed, fabricated, and presented by several groups [14–20]. In VSRR structures, the SRR array is standing rather than lying

on the substrate, which gives rise to a strong interaction with the incidence magnetic field. This intriguing framework provides a new route to obtain a strong magnetic response to the impinging light incidence from the top of the metamaterials [16].

Terahertz metamaterial sensing systems are important applications owing to their attractive potential for identifying and detecting minute amounts of chemical and biochemical substances [21]. These promising sensing tasks are generally accomplished by measuring the resonant response differences of the metamaterials, such as shifts of the position and depth of the resonance, caused by the analyte approaching them [21]. When the analyte is overlaid on top of the metamaterials, the changed resonant responses are translated into pronounced alterations of transmission/reflection signals in the response spectra [22]. As these changes can be directly detected, this offers an effective method to determine the attributes of the analyte, like the mass centration of a biochemical compound, by studying the changes of the resonance of the metamaterials [21]. Thus, the performance of metamaterial sensing systems could be improved in two aspects [22]. The first is exploration of the resonances of higher quality (Q) factor that have extremely narrow linewidth [23–27]. The other is realization of higher sensitivity to the attributes of the nearby analyte, such as a larger shift of resonant frequency position.

In this paper, an ultrasensitive metamaterial sensor based on a double-slot VSRR (DVSRR) is proposed and numerically analyzed in the terahertz frequency. The standing framework of the DVSRR array produces a strong fundamental magnetic resonance driven purely by the incidence magnetic field [14]. Also, in the DVSRR array design suggested in this paper, half of the spots of electric field enhancement are surrounded with air rather than substrate material, which enormously reduces the dielectric loss resulting from the substrate. This is the main reason why the DVSRR sensor has much higher sensitivity than planar SRR counterparts. In addition, the robustness of the sensing performance of the DVSRR sensor is evaluated with the fabrication tolerance and a wide range of incidence angles under TE and TM incidence radiation [28].

2. SENSOR DESIGN

Figure 1 presents the proposed VSRR metamaterial sensor configuration and the amplifying view of a single unit cell used in the simulation. The numerical calculations are performed using the frequency domain solver of the commercial EM wave solver CST Microwave Studio. The period of the simulated square unit cell is $p = 70$ μm. The aluminum ($\sigma = 3.56 \times 10^7$ S/m) DVSRRs have two slots in the top and bottom metal plates. The width of the two slots is equal and marked as $g = 2$ μm. The length and width of two metal (top and bottom) plates are $a = 50$ μm and $b = 12$ μm, respectively. All the metal plates share the same thickness, $t = 1$ μm. The top and bottom plates are separated by two metal cylinders with height $h = 30$ μm and radius $r = 6$ μm. The metal structure is built on top of a polyimide ($\varepsilon = 3.5 + 0.00945i$) substrate, and the numerically calculated thickness of the substrate is $d = 40$ μm. As shown in the inset of Fig. 1, the incident light is impinging normal to the top surface of the metamaterial sensor along the z axis of

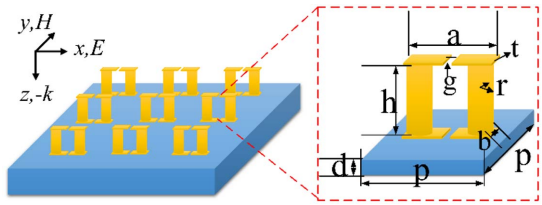

Fig. 1. 3D schematic drawing of the proposed metamaterial sensor and a single enlarged unit cell with its geometrical dimensions. The inset shows the polarization of the EM wave illumination. The electric field component is vertical to the gap of the DVSRRs. The magnetic field is normal to the DVSRR. The EM wave illuminates from the top perpendicularly. The geometric parameters of a single DVSRR unit cell are $a = 50$ μm, $b = 12$ μm, $t = 1$ μm, $h = 30$ μm, $r = 6$ μm, and $g = 2$ μm. The period of the square lattice is $p = 70$ μm.

the coordinate system. The E field along the x axis is perpendicular to the gap of the VSRR array, and the H field passes through the DVSRR vertically.

The numerically calculated transmission spectrum of the DVSRR is presented in Fig. 2, along with the transmission spectra of two other VSRR frameworks for comparison. These three VSRRs share the same geometric dimensions, except for the position and number of gaps. The presented TVSRR and BVSRR are VSRRs with only a top or bottom gap, respectively. All the curves in Fig. 2 have been normalized by the transmission of a bare polyimide with the same thickness $d = 40$ μm. As shown in Fig. 2, the transmission curves show the remarkable differences in the position and Q-factor of the resonance. For the DVSRR, the transmission dip is at 1.5102 THz and the Q-factor is about 20. By contrast, the Q-factors of the TVSRR and BVSRR are only 4.38 and 2.61. The central frequencies of their resonant dips are 0.9853 and 0.7305 THz, respectively.

To better explore the physics behind the resonant characteristics of the three VSRRs, the distributions of the surface currents and the electric and magnetic energy densities are studied by numerical calculations at the resonant positions and shown in Fig. 3. It can be observed from the subgraphs in the first and second columns of Fig. 3 that the circulating currents form on

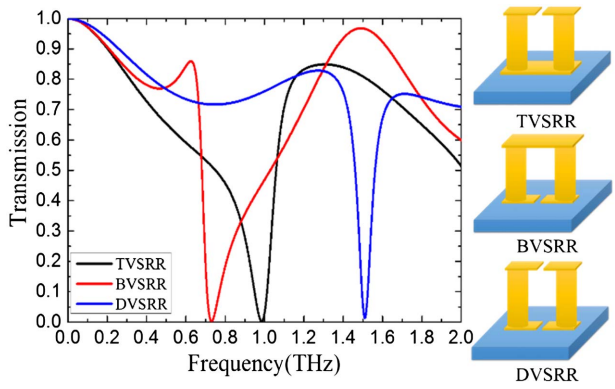

Fig. 2. Comparison of the transmission spectra of three different VSRRs that share the same dimensions, except for the positions and number of gaps. The TVSRR and BVSRR display the VSRRs with one slot in the top or bottom metal plate, respectively.

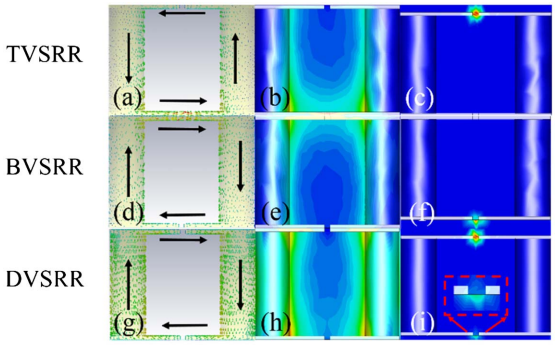

Fig. 3. Comparison of the numerically calculated distributions of the three VSRR structures at resonant frequencies, namely 0.9853, 0.7305, and 1.5102 THz for TVSRR, BVSRR, and DVSRR respectively. (a), (d), and (g) illustrate the surface current distributions for the three VSRRs. The black arrows denote the directions of surface electric current. (b), (e), and (h) show the magnetic energy density distributions. The electric energy density distributions are also shown in (c), (f), and (i). The electric energy density in the lower gap of the DVSRR is enlarged and demonstrated in the red dotted line box in the inset of (i).

the surface of the VSRR structures and most of the magnetic energy is concentrated within them, which implies that the resonances in Fig. 2 are all fundamental *LC* resonance [17]. The electric energy density distributions shown in the third column of Fig. 3(c) illustrate that the electric fields are centered mainly in the gaps of the VSRRs and, thus, are significantly enhanced. Both the TVSRR and BVSRR have one single high field region, but the intensity for the BVSRR is much lower than that of the TVSRR. This difference results from more plasmon field permeating into the substrate in the case of the BVSRR, which increases the dielectric loss and thus decreases its sensing potentials [29]. For the DVSRR, two high field regions are shown, and the inset in Fig. 3(i) shows that the field intensity in the lower gap is also suppressed by the substrate. According to the equivalent circuit model, which is a widely accepted approach to qualitatively describe the position of *LC* resonance in line with the relationship $\omega_{\mathrm{LC}} \propto (LC)^{-1/2}$ [30], the inductance plays no role in the resonant position due to small variations in the geometric structures among the three VSRRs. Thus, following the law of causality, the change of the capacitance contributes mostly to the resonant frequency differences. The two gaps of the DVSRR can be equivalent as two series capacitance, which effectively reduces the total capacitance of the structure, and, therefore, the resonant frequency of the DVSRR lies at the right side of the others. For the TVSRR and BVSRR, although both have one single slot in their unit cells, the distinct dielectric surroundings create differences in the effective capacitance. That is to say, the substrate material (polyimide) near the BVSRR gap has a higher permittivity than the air close to the TVSRR gap, which increases the effective capacitance of the BVSRR [30] and thus leads to a lower resonant frequency for the BVSRR compared to the TVSRR.

The *Q*-factor of the resonance for the DVSRR is more than 4 times those of the other two VSRR structures. This prominent difference can be attributed to the introduction of bianisotropy in the TVSRR and BVSRR resulting from their asymmetric structures [15]. It is well established that the SRR is intrinsically bianisotropic owing to the absence of inversion symmetry in the structural plane [31]. As displayed in the insets of Fig. 2, symmetry breaking occurs in the TVSRR and BVSRR structures along the incidence direction of the EM wave, which introduces the bianisotropy. For the DVSRR, inversion symmetry along the z axis has been realized. Although the presence of the substrate will introduce weak bianisotropy, it is so trivial that it can be ignored [17]. Specifically, it is well known that the *LC* resonance of the SRR could be activated through either an electric-coupling-induced capacitance response or a magnetic-coupling-induced inductance response [32]. When the EM wave is polarized as indicated in Fig. 1, both the electric and magnetic field components could excite the *LC* resonance in the three VSRR structures, which introduces a strong bianisotropy effect and, therefore, distorts and broadens their transmission curves. However, for the DVSRR, electric excitation cannot work well due to the structure symmetry, thus the magnetic field plays a predominantly important role in the excitation of the *LC* resonance [17]. Therefore, the *LC* resonance of the DVSRR is a purely magnetic excitation mode, and the bianisotropy introduced by the illumination orientation is eliminated. From the perspective of electrodynamics, in the case of the DVSRR, there are two electric dipoles occurring at the gaps and one magnetic dipole normal to the DVSRR [17]. These two electric dipoles are 90° out of phase, which can be treated as an electric quadrupole. The radiation damping produced by the contribution of the electric quadrupole and magnetic dipole is relatively low and, therefore, the *Q*-factor of the resonance is highly improved. However, in the cases of the TVSRR and BVSRR, only one electric dipole is produced at their respective gaps and thus plays a dominant role in the contribution of the radiation loss [17], which dramatically decreases the *Q*-factor of the resonances for the TVSRR and BVSRR.

3. SENSING CAPACITY EVALUATION AND ANALYSIS

The performance of the metamaterial sensor based on the DVSRR will be demonstrated and evaluated in this section. The schematic diagram of the coupling process between the analyte and the DVSRR system is plotted in Fig. 4(a). The analyte added on top of the sensor could be a gaseous or liquid material containing substances like DNA and glucose. Figure 4(b) shows the transmission spectral comparison of the simulated sensing processes induced by various analyte thicknesses and a fixed RI $n = 1.6$. This particular RI is chosen as it appears in many papers [22,26,33]. The fitting curve of the thickness sensing using the data shown in Fig. 4(b) is displayed in Fig. 4(d). With the thickness of the analyte increasing gradually, the central frequency of the resonant dip occurs a continuous redshift as the effective capacitance increases due to the introduction of the dielectric material filling the gaps of the DVSRR [30]. However, this phenomenon persists only when the thickness is less than 5 μm. Both from Figs. 4(b) and 4(d) it can be observed that the frequency shift (FS) tends to saturate when the thickness reaches above 5 μm. The FS caused by the

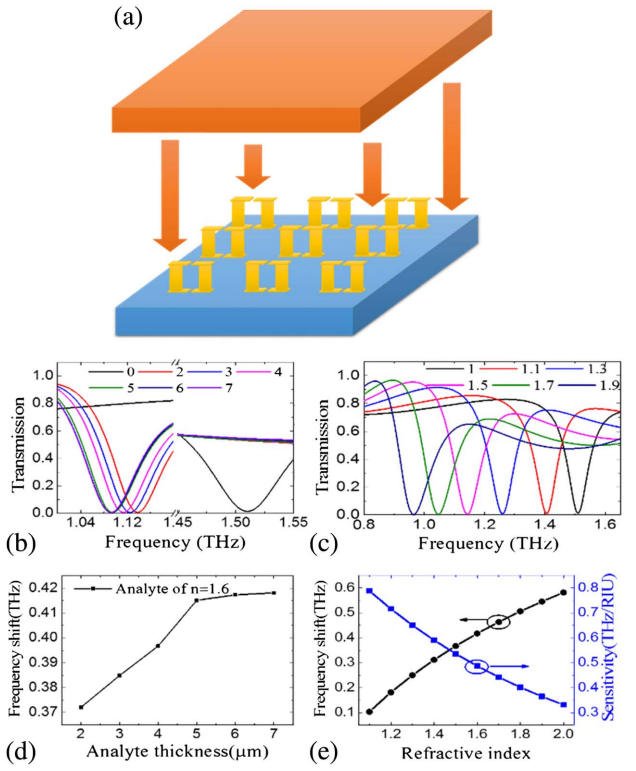

Fig. 4. (a) 3D sketch diagram of the sensing configuration including the DVSRR's array sensor and analyte. The sensing performance based on the thicknesses and RIs of the analyte are shown in the following subgraphs. (b) The transmission spectra of the DVSRR with and without analyte overlaid on the sensor. Analytes with the different thicknesses (l = 2–7 μm) and constant n = 1.6 are used in the numerical calculations of (b). To observe more clearly the sensing evolution, a break for the coordinate values in the horizontal axis has been introduced. (d) The fitting function using the data from (b) between the FS of the resonant dip and analyte thickness are shown. (c) Different transmission spectra are induced by the increasing RI (n = 1–1.9) and constant l = 6 μm of the analyte. (e) The exponential fitting curve for the data shown in (c) are displayed as the black curve, which can be expressed as FS = 0.92464 – 2.326035 ∗ exp(–0.96198 ∗ n) with R^2 = 0.99992. The RI sensitivity of the DVSRR is also displayed as the blue curve in (e).

saturated thickness l = 6 μm and n = 1.6 of the analyte is 417 GHz, as shown in Fig. 4(d). A similar saturation phenomenon of thickness sensing is also seen in other researchers' work, but the saturated thicknesses are larger there [22,30]. This shows that the EM field of the DVSRR sensing scheme can stretch much closer than previous sensors. In addition, the considerable FS induced by the minor thickness provides a good indication of the superior sensitivity of the DVSRR structure.

For the RI sensing, the constant saturated thickness l = 6 μm is employed and a sweep of simulations is conducted from n = 1.1–2. As shown in Fig. 4(c), the frequency positions of the transmission minima show redshifts as well with the increasing RI. The fitting curve for the RI sensing is displayed in Fig. 4(e). Interestingly, the fitting curve is no longer a straight line, which is a common case and has been proven by several groups [22,26,33]. A linear fitting attempt for the same data has been performed (the result is not shown) and the goodness of fit is merely R^2 = 0.9838, which is much inferior to the exponential fitting result. This nonlinearity might be indicative that stronger couplings take place in the DVSRR sensing configuration, which leads to the occurrence of outstanding sensitivity for the DVSRR sensing system. As shown in Fig. 4(e), the maximum shift of the central frequency of the dip is 582 GHz when the analyte is laid on top of the sensor with thickness l = 6 μm and n = 2. As the fitting curve of the RI sensing is not a straight line, the RI sensitivity decreases gradually from 788 to 332 GHz/RIU, as illustrated by the blue curve in Fig. 4(e). These numbers can be converted into $\Delta\lambda$/RIU by using $|d\lambda/dn| = c_0/f_0^2 * df/dn$, where c_0 is the speed of the light in vacuum, f_0 is the resonance frequency, λ is the wavelength, and n denotes the RI. At this rate, the RI sensitivity ranges from 4.37×10^4 to 1.04×10^5 nm/RIU. All these data show the sensitivity of the DVSRR is significantly better than other results in terahertz sensing applications [21–24,26,33,34]. In particular, the DVSRR structure provides a superb sensing platform for sensing the analyte with the lower RI. For example, the RI of DNA varies from 1.4 to 1.6 [22] and, in this case, the sensitivity can stay at a high level of 6.41×10^4 to 7.77×10^4 nm/RIU.

To get a deep insight into the mechanism leading to this superior sensitivity, the sensing levels of the three VSRR structures are compared. As demonstrated in Figs. 5(a) and 5(b), the sensing level of the BVSRR structure is far lower than those of the others. The reasons for the obvious sensitivity differences are the position and number of gaps, as they are the only differences among the three VSRR structures. Since the gap of the BVSRR is deposited on the substrate, this will result in considerable electric energy loss introduced by the substrate [26,29]. This can be proven by Figs. 3(c), 3(f), and 3(i); the electric energy density in the top gap is far stronger than that in the bottom gap. Additionally, the highly confined electric field in the gap plays a crucial role in the SRR structure's sensing.

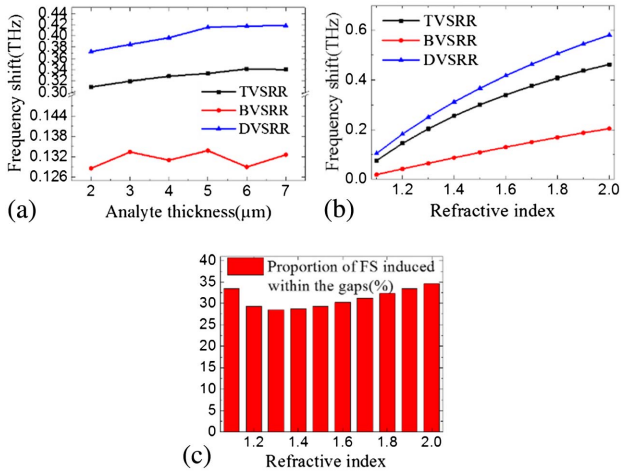

Fig. 5. Comparative plots of (a) thickness sensing with fixed RI of n = 1.6 and (b) RI sensing with constant thickness l = 6 μm among the three structures: TVSRR, BVSRR, and DVSRR. A break is added in the y axis of (a) to manifest the values of FS for different VSRRs. (c) The bar plot shows the proportion of FS for n = 1.1–2 induced by the analyte filling within the two gaps of DVSRR.

Thus, due to the existence of high dielectric loss, the sensing performance of the BVSRR is unremarkable. Furthermore, that the top gaps in the TVSRR and DVSRR contact with the air, which has a lower RI than the substrate, makes a dominant contribution to the sensing performance improvement. The central frequency position of LC resonance is located according to $\omega = 1/\sqrt{LC}$. In the sensing process, the analyte replaces the air close to the gaps when approaching the sensor and thus changes the effective capacitance on the basis of $\varepsilon = \varepsilon_{\text{eff}} + \alpha(\varepsilon_{\text{analyte}} - 1)$ and $C = \varepsilon * A/d$ [35], where ε_{eff} is the effective permittivity of the substance near the gaps, and A and d are geometric parameters of the capacitor. Since the analyte has a larger permittivity than air, the resonant dip redshifts when the analyte is laid on top of the sensor. The FS induced by the approaching analyte can be expressed as

$$\Delta f = f_0 - f = \sqrt{\frac{d}{2\pi LA}} * \frac{1}{\sqrt{\varepsilon_{\text{eff}}}} * \left[1 - \frac{1}{\sqrt{1 + \alpha(\varepsilon_{\text{analyte}} - 1)/\varepsilon_{\text{eff}}}}\right]. \quad (1)$$

It can be inferred from Eq. (1) that the smaller is the effective permittivity of the substance close to the gaps, the larger is the FS that will be induced. Therefore, VSRR structures having gaps surrounded by air instead of the substrate material will show better sensitivity. On the other hand, as demonstrated in Figs. 4(c) and 4(i), the gap existing in the bottom of the DVSRR structure, which also contributes to the sensitivity enhancement, ensures better sensing performance than that of the TVSRR. It is worth noting that the curvature of the RI sensing curve for the TVSRR in Fig. 5(b) is the largest, and the curve for BVSRR is as smooth as a straight line, whereas the curvature for the DVSRR appears just between theirs. Hence, it can be inferred that the top gap in the VSRR structures is a crucial factor for producing the nonlinear RI sensing line, as shown in Fig. 4(e). Figure 5(c) demonstrates the proportion of the FS induced by analyte only filling within the gaps of the DVSRR compared to the FS produced by the analyte fully overlaid on the sensor, as shown in Fig. 4(a). The FS proportion is about 30% for the whole RI range, while the volume of the analyte filling within the gaps occupies only 0.0325% of the total volume of the analyte fully covering the sensor. Combined with previous discussion, this clearly shows that the gaps, especially the top gap, play a significantly important role in the excellent sensitivity of the DVSRR sensor. In this sense, the DVSRR sensor not only provides ultrasensitivity to the analyte, but also promises the detection of minute amounts of matter such as bacteria and fungi [35].

Solid sensing represents the sensing application for solid materials. Under this circumstance, this unflowing matter cannot penetrate inside the sensor as far as the gaseous/liquid ones. Thus, the performance of the DVSRR sensing system for a solid analyte will notably degrade owing to insufficient contact between the analyte and highly confined field gap. Some simulations have been conducted to determine the sensing performance for solid sensing. The results show the FS is just 207 GHz when a solid analyte with $n = 1.6$ and $l = 6$ μm is deposited on top of the sensor. For RI sensing, the fitting line is almost a straight line with a goodness of fit of $R^2 = 0.99447$. The RI sensitivity, which is the slope of the fitting straight line, is 288 GHz/RIU or 3.79×10^4 nm/RIU. All these numbers reveal that although the DVSRR sensing platform shows a much reduced sensitivity for solid sensing, it is still able to display excellent sensing performance.

4. ROBUSTNESS ANALYSIS

In the fabrication process of the metamaterials, there will be unavoidable inaccuracy in their structural dimensions due to limitations of the fabrication technology. These inaccuracies can be errors in the thickness and width of the metal film or the roughness of the metal surface relative to the theoretically designed structure. All these structural size deviations would lead to property changes of the metamaterials with respect to the originally designed ones. Thus, the property changes of the DVSRR induced by fabrication imperfections are studied and demonstrated in Fig. 6. Figure 6(a) displays the transmission spectral comparison of the DVSRRR with fabrication tolerance ranging from −4% to 4%. This range denotes the extent of the error percentage of all the structural dimensions of the DVSRR relative to the originally designed DVSRR. It can be seen from Fig. 6(a) that the transmission curves show nearly no difference except for the slight shifts of the central frequency position and amplitude of the resonance. The maximum shift of the resonant position is 2.83% or 43 GHz with respect to the designed resonance frequency of 1.5102 THz when the fabrication tolerance is 4%. The impact of the fabrication tolerance on the Q-factor of the resonance is shown as the blue curve in Fig. 6(b). The Q decreases from 20.41 to 17.88 when the fabrication tolerance ranges from −4% to 4%. The influence of fabrication imperfections on the sensing performance of the DVSRR is displayed as the black curve in Fig. 6(b). The maximum deviation relative to the original FS (417 GHz) induced by the analyte with $n = 1.6$ and $l = 6$ μm is 18 GHz or 4.41% when the fabrication tolerance is 2%. All these data shown in Fig. 6 illustrate that the DVSRR structure can maintain well with the fabrication tolerance ranging from −4% to 4%, particularly its sensing performance.

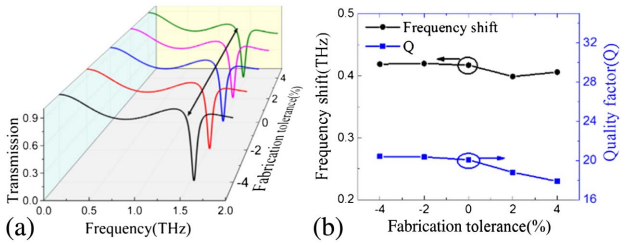

Fig. 6. (a) 3D schematic drawing of the transmission spectral comparison for various DVSRR structures with fabrication tolerance ranging from −4% to 4%. Fabrication toleration is supposedly induced by inaccuracy in the fabrication process, which is calculated as a common coefficient of all the structural dimensions of the DVSRR. The sign "±" represents enlarging or shrinking all the structural dimensions of the DVSRR. (b) The Q-factor of the resonance of the DVSRR is shown as a function of fabrication tolerance (blue curve). The black curve shows the FS of its resonance dip induced by the analyte with $n = 1.6$ and thickness $l = 6$ μm versus fabrication tolerance.

Figures 7(a) and 7(b) demonstrate the evolution of the *LC* resonance transmission spectra of the DVSRR under TM and TE illumination, respectively, with the incidence angle increasing from 0° to 50°. The step of the incidence angle sweep employed in the simulation is 10°. The two plots demonstrate that the spectral characteristics maintain well near the resonance position under the two illumination configurations for a wide range of incidence angles, which can be up to 50°. The transmission curves show slight redshift with increasing incidence angles. The maximum shift of the central frequency position of the resonance is only 1.27% or 19 GHz for TM illumination and 0.94% or 14 GHz for TE illumination with incidence angle of 50°. The sensing features of the DVSRR system under TM and TE illumination with incidence angles ranging from 0° to 50° are displayed in Fig. 8. The impact of the incidence angles on the sensing perform are studied by numerical calculations with analyte of $n = 1.2$–2 with a step of 0.2 and fixed $l = 6$ μm deposited on top of the sensor. Figures 8(a) and 8(b) show the evolution of the sensing performance with increasing incidence angles and RI for two different incidence radiations. For each RI in the range of $n = 1.2$–2, the FS stays almost constant for the increasing angles, which can be inferred from the almost unchanged height of the color bars in Figs. 8(a) and 8(b). The color bars show the value range of the FS induced by the various analytes. The legend shown in Fig. 8(a) is shared by the two 3D bar plots, in which various colors represent the extent (about 0.05 THz) of the FS. To more clearly display the incidence angle insensitivity of the DVSRR, the sensing performance when analyte of $n = 1.6$ and $l = 6$ μm is laid on top of the sensor is randomly selected as an example. As shown in Fig. 8(c), the FS gradually decreases with increasing incidence angles for the two different incidence radiations. However, the resultant maximum deviations of the FS are just 3.64% or 15 GHz for TM illumination and 2.38% or 10 GHz for TE illumination when the incidence angle is 50°, which illustrates that the sensing performance of the DVSRR is insensitive to incidence angles up to 50°. It is worth noting that, as displayed in Fig. 8(c), the FS for the two illuminations under normal incidence should have been the same, but the FS is 415 GHz rather than 417 GHz for TM illumination. This slight discrepancy is caused by a numerical calculation error by the EM wave solver software.

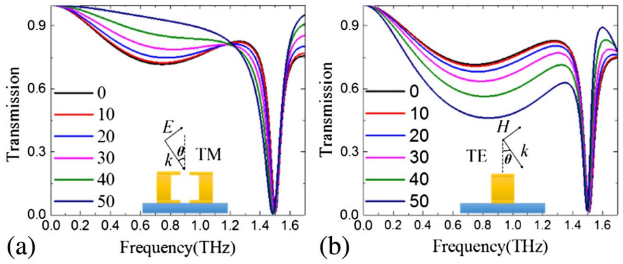

Fig. 7. Transmission spectral comparison for (a) TM and (b) TE incidence radiation with increasing incidence angles with a step of 10°. The polarizations of the two incidence radiations are shown as the insets in (a) and (b).

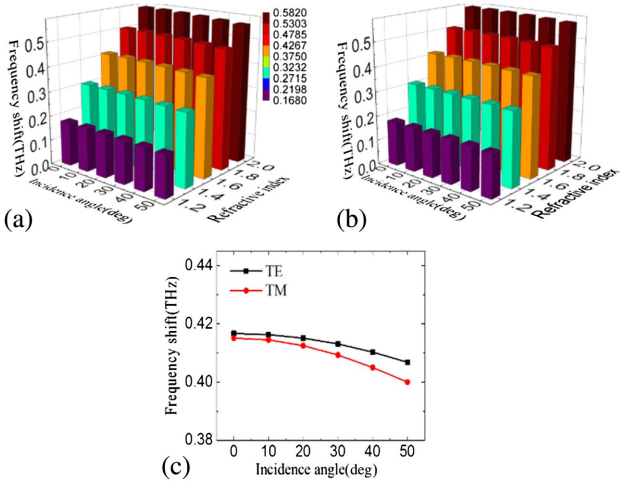

Fig. 8. 3D bar plots shows the evolution of the sensing performance of the DVSRR for a wide range of incidence angles (0°–50°) and the increasing RI (1.2–2) with fixed thickness $l = 6$ μm under (a) TM and (b) TE incidence radiation. (c) The numerically calculated results of the FS induced by the analyte with $n = 1.6$ and $l = 6$ μm are shown as a function of the incidence angles for the TM and TE illumination, selected as examples to illustrate that the sensing performance of the DVSRR is incidence-angle-insensitive in the range of 0°–50°.

5. CONCLUSION

In conclusion, a type of standup metamaterials used for sensing is designed in the terahertz bands. This double-split SRR design not only eliminates bianisotropy to induce an *LC* resonance of high *Q*-factor, but also sharply reduces the dielectric loss induced by the substrate, which leads to superior sensitivity for determining analytes. For these reasons, the DVSRR sensor performs much better than the traditional planar metamaterial sensors and can maintain its excellent sensing feature for a wide incidence angle up to 50° and exhibits fabrication tolerance. This sensing system provides a new route to achieve high sensitivity and an additional degree of freedom for designing and tuning. Because of the universality of the metamaterial resonant response, this research work can be applied to designing various metamaterial-based devices using the strong magnetic response of the VSRR structure.

Funding. National Natural Science Foundation of China (NSFC) (61327006, 61620106014).

REFERENCES

1. J. B. Pendry, A. J. Holden, W. J. Stewart, and I. I. Youngs, "Extremely low frequency plasmons in metallic mesostructures," Phys. Rev. Lett. **76**, 4773–4776 (1996).
2. J. B. Pendry, A. J. Holden, D. J. Robbins, and W. J. Stewart, "Magnetism from conductors and enhanced nonlinear phenomena," IEEE Trans. Microw. Theory Tech. **47**, 2075–2084 (1999).
3. D. R. Smith, S. Schultz, P. Markos, and C. M. Soukoulis, "Determination of effective permittivity and permeability of metamaterials from reflection and transmission coefficients," Phys. Rev. B **65**, 195104 (2002).
4. R. Marqués, J. Martel, F. Mesa, and F. Medina, "Left-handed-media simulation and transmission of EM waves in subwavelength

split-ring-resonator-loaded metallic waveguides," Phys. Rev. Lett. **89**, 183901 (2002).
5. Z. G. Dong, S. N. Zhu, H. Liu, J. Zhu, and W. Cao, "Numerical simulations of negative-index refraction in wedge-shaped metamaterials," Phys. Rev. E **72**, 016607 (2005).
6. T. Koschny, P. Markos, D. R. Smith, and C. M. Soukoulis, "Resonant and antiresonant frequency dependence of the effective parameters of metamaterials," Phys. Rev. E **68**, 065602 (2003).
7. S. Tan, F. Yan, L. Singh, W. Cao, N. Xu, X. Hu, R. Singh, M. Wang, and W. Zhang, "Terahertz metasurfaces with a high refractive index enhanced by the strong nearest neighbor coupling," Opt. Express **23**, 29222–29230 (2015).
8. N. I. Landy, S. Sajuyigbe, J. J. Mock, D. R. Smith, and W. J. Padilla, "Perfect metamaterial absorber," Phys. Rev. Lett. **100**, 207402 (2008).
9. H.-T. Chen, J. Zhou, J. F. O'Hara, F. Chen, A. K. Azad, and A. J. Taylor, "Antireflection coating using metamaterials and identification of its mechanism," Phys. Rev. Lett. **105**, 073901 (2010).
10. T. J. Yen, W. J. Padilla, N. Fang, D. C. Vier, D. R. Smith, J. B. Pendry, D. N. Basov, and X. Zhang, "Terahertz magnetic response from artificial materials," Science **303**, 1494–1496 (2004).
11. S. Linden, C. Enkrich, M. Wegener, J. Zhou, T. Koschny, and C. M. Soukoulis, "Magnetic response of metamaterials at 100 terahertz," Science **306**, 1351–1353 (2004).
12. N. Katsarakis, G. Konstantinidis, A. Kostopoulos, R. S. Penciu, T. F. Gundogdu, M. Kafesaki, E. N. Economou, T. Koschny, and C. M. Soukoulis, "Magnetic response of split-ring resonators in the far-infrared frequency regime," Opt. Lett. **30**, 1348–1350 (2005).
13. R. A. Shelby, D. R. Smith, and S. Schultz, "Experimental verification of a negative index of refraction," Science **292**, 77–79 (2001).
14. W. T. Chen, C. J. Chen, P. C. Wu, S. Sun, L. Zhou, G.-Y. Guo, C. T. Hsiao, K.-Y. Yang, N. I. Zheludev, and D. P. Tsai, "Optical magnetic response in three-dimensional metamaterial of upright plasmonic meta-molecules," Opt. Express **19**, 12837–12842 (2011).
15. K. Fan, A. C. Strikwerda, H. Tao, X. Zhang, and R. D. Averitt, "Stand-up magnetic metamaterials at terahertz frequencies," Opt. Express **19**, 12619–12627 (2011).
16. P. C. Wu, W. T. Chen, K. Y. Yang, C. T. Hsiao, G. Sun, A. Q. Liu, N. I. Zheludev, and D. P. Tsai, "Magnetic plasmon induced transparency in three-dimensional metamolecules," Nanophotonics **1**, 131–138 (2012).
17. K. Fan, A. C. Strikwerda, X. Zhang, and R. D. Averitt, "Three dimensional broadband tunable terahertz metamaterials," Phys. Rev. B **87**, 161104 (2013).
18. P. C. Wu, G. Sun, W. T. Chen, K. Y. Yang, Y. W. Huang, Y. H. Chen, H. L. Huang, W. L. Hsu, P. C. Hai, and D. P. Tsai, "Vertical split-ring resonator based nanoplasmonic sensor," Appl. Phys. Lett. **105**, 033105 (2014).
19. P. C. Wu, W.-L. Hsu, W. T. Chen, Y.-W. Huang, C. Y. Liao, A. Q. Liu, N. I. Zheludev, G. Sun, and D. P. Tsai, "Plasmon coupling in vertical split-ring resonator metamolecules," Sci. Rep. **5**, 9726 (2015).
20. D. Liang, H. Zhang, J. Gu, Y. Li, Z. Tian, C. Ouyang, J. Han, and W. Zhang, "Plasmonic analog of electromagnetically induced transparency in stereo metamaterials," IEEE J. Sel. Top. Quantum Electron. **23**, 4700907 (2017).
21. T. Chen, S. Li, and H. Sun, "Metamaterials application in sensing," Sensors **12**, 2742–2765 (2012).
22. L. Cong, S. Tan, R. Yahiaoui, F. Yan, W. Zhang, and R. Singh, "Experimental demonstration of ultrasensitive sensing with terahertz metamaterial absorbers: a comparison with the metasurfaces," Appl. Phys. Lett. **106**, 031107 (2015).
23. C. Debus and P. H. Bolivar, "Frequency selective surfaces for high sensitivity terahertz sensing," Appl. Phys. Lett. **91**, 184102 (2007).
24. I. A. I. Al-Naib, C. Jansen, and M. Koch, "Thin-film sensing with planar asymmetric metamaterial resonators," Appl. Phys. Lett. **93**, 083507 (2008).
25. N. Liu, T. Weiss, M. Mesch, L. Langguth, U. Eigenthaler, M. Hirscher, C. Sönnichsen, and H. Giessen, "Planar metamaterial analogue of electromagnetically induced transparency for plasmonic sensing," Nano Lett. **10**, 1103–1107 (2010).
26. R. Singh, W. Cao, I. Al-Naib, L. Cong, W. Withayachumnankul, and W. Zhang, "Ultrasensitive terahertz sensing with high-Q Fano resonances in metasurfaces," Appl. Phys. Lett. **105**, 171101 (2014).
27. I. Al-Naib, E. Hebestreit, C. Rockstuhl, F. Lederer, D. Christodoulides, T. Ozaki, and R. Morandotti, "Conductive coupling of split ring resonators: a path to THz metamaterials with ultrasharp resonances," Phys. Rev. Lett. **112**, 183903 (2014).
28. H. Tao, C. M. Bingham, A. C. Strikwerda, D. Pilon, D. Shrekenhamer, N. I. Landy, K. Fan, X. Zhang, W. J. Padilla, and R. D. Averitt, "Highly flexible wide angle of incidence terahertz metamaterial absorber: design, fabrication, and characterization," Phys. Rev. B **78**, 241103 (2008).
29. A. Dmitriev, C. Hägglund, S. Chen, H. Fredriksson, T. Pakizeh, M. Käll, and D. S. Sutherland, "Enhanced nanoplasmonic optical sensors with reduced substrate effect," Nano Lett. **8**, 3893–3898 (2008).
30. T. Driscoll, G. O. Andreev, D. N. Basov, S. Palit, S. Y. Cho, N. M. Jokerst, and D. R. Smith, "Tuned permeability in terahertz split-ring resonators for devices and sensors," Appl. Phys. Lett. **91**, 062511 (2007).
31. R. Marqués, F. Medina, and R. Rafii-El-Idrissi, "Role of bianisotropy in negative permeability and left-handed metamaterials," Phys. Rev. B **65**, 144440 (2002).
32. N. Katsarakis, T. Koschny, M. Kafesaki, E. N. Economou, and C. M. Soukoulis, "Electric coupling to the magnetic resonance of split ring resonators," Appl. Phys. Lett. **84**, 2943–2945 (2004).
33. I. Al-Naib, "Biomedical sensing with conductively coupled terahertz metamaterial resonators," IEEE J. Sel. Top. Quantum Electron. **23**, 4700405 (2017).
34. S.-Y. Chiam, R. Singh, J. Gu, J. Han, W. Zhang, and A. A. Bettiol, "Increased frequency shifts in high aspect ratio terahertz split ring resonators," Appl. Phys. Lett. **94**, 064102 (2009).
35. S. J. Park, J. T. Hong, S. J. Choi, H. S. Kim, W. K. Park, S. T. Han, J. Y. Park, S. Lee, D. S. Kim, and Y. H. Ahn, "Detection of microorganisms using terahertz metamaterials," Sci. Rep. **4**, 4988 (2014).